ELSEVIER

Journal of Nuclear Materials 306 (2002) 180–189

journal of nuclear materials

www.elsevier.com/locate/jnucmat

# Helium behaviour and defect evolution in amorphous spinel during thermal annealing

P.M.G. Damen [a,*], A. van Veen [b], Hj. Matzke [a], H. Schut [b], J.A. Valdez [c], C.J. Wetteland [c], K.E. Sickafus [c]

[a] *European Commission, Joint Research Centre, Institute for Transuranium Elements, P.O. Box 2340, D-76125 Karlsruhe, Germany*

[b] *Interfaculty Reactor Institute, Delft University of Technology, Mekelweg 15, 2629 JB Delft, The Netherlands*

[c] *Materials Science and Technology Division, Los Alamos National Laboratory, Los Alamos, NM 87545, USA*

Received 20 June 2002; accepted 17 September 2002

**Abstract**

$MgAl_2O_4$-spinel has been widely investigated as inert matrix for actinide-transmutation. Under impact of fission fragments, it becomes amorphous. During reactor irradiation, crystalline and amorphous spinel are expected in the fuel, containing, among others xenon and helium. Gas-release measurements and positron beam analysis (PBA) were performed on amorphized specimens and compared to results on crystalline spinel. Helium was released in two stages between 575 and 800 K in first-order desorption processes with activation enthalpies of 1.9 and 2.7 eV and attempt frequencies of about $10^{13}$ $s^{-1}$. Xenon was released between 1050 and 1450 K. PBA experiments indicated that defect clustering occurred near the surface at low temperatures and in deeper regions at about 950–1200 K. Recrystallization was observed between 1000 and 1350 K and defect annealing was completed at 1600 K. PBA indicates two different damage zones, corresponding to displacement zones with and without xenon.



## 1. Introduction

In many oxides that are turned amorphous under impact of energetic heavy rare gas ions, such as $Al_2O_3$, $TiO_2$, $U_3O_8$, $SiO_2$ etc., the gas is swept out and released during recrystallization, hence at much lower temperatures than those for gas release from the crystalline oxides [1]. The question is open whether this is also true for helium, which is expected to be released at lower temperatures from the crystalline oxides than the fission gases krypton and xenon.

Spinel ($MgAl_2O_4$) has received considerable attention as a potential inert matrix material because of its relatively high thermal conductivity and its good stability against neutron and α-particle damage [2]. However, spinel has been shown sensitive to swelling as well as to succumb to an amorphization transformation under impact of fission products [3]. Following the EFTTRA experiments [4], interest began to grow in the interplay between helium gas build-up in the fuel (helium gas is formed in the matrix through α-decay) and helium mobility in a spinel matrix that becomes increasingly amorphous due to fission product damage. So far, many studies have been performed on the behaviour of helium and rare gases in both single-crystal and polycrystalline spinel [5–9]. However, the behaviour of helium and xenon in an initially amorphous spinel matrix has not been studied so far.

The present work was therefore initiated to investigate the following processes:

- helium release from amorphous spinel, compared with results for crystalline spinel;

* Corresponding author. Tel.: +49-7247 951 486; fax: +49-7247 951 198/99650.

*E-mail address:* damen@itu.fzk.de (P.M.G. Damen).

0022-3115/02/$ - see front matter 
PII: S0022-3115(02)01259-X

- xenon release from amorphous spinel, compared with results for crystalline spinel;
- helium and xenon release during recrystallization;
- defect formation and annealing in the presence of helium and xenon.

In this paper, the above mentioned processes will be discussed and whenever possible, comparisons between amorphous and single/polycrystalline spinel will be made.

## 2. Experimental procedure

### 2.1. Sample preparation

Spinel ($MgAl_2O_4$) single-crystal substrates of union carbide, with (1 1 1) orientation were implanted at the Los Alamos Ion-Beam Materials Laboratory with 450 keV $Xe^{3+}$ ions at cryogenic temperature (100 K). This procedure has been shown to yield an amorphous layer on the spinel specimen [10]. Under more realistic conditions, amorphous spinel can be formed by swift heavy ions [11]. The samples were tilted 7° relative to the normal beam incidence to decrease channelling. The implantation was performed with a flux of $8 \times 10^{11}$ Xe $cm^{-2}\,s^{-1}$ up to a total dose of $1 \times 10^{16}$ Xe $cm^{-2}$. A second implantation on the same surface was performed with 14 keV $He^+$-ions at the same temperature where the sample was tilted 61° relative to the normal beam incidence in an attempt to deposit helium at approximately half of the depth of the xenon layer. The implantation flux used was $7 \times 10^{12}$ He $cm^{-2}\,s^{-1}$ up to a total implanted dose of $1 \times 10^{15}$ He $cm^{-2}$.

### 2.2. Damage distribution and implantation profile

TRIM [12] (version: SRIM-2000.10) calculations were performed with threshold displacement energies of 30/30/60 eV for Mg/Al/O [6]. The results of the TRIM calculations are shown in Fig. 1. The calculations show a maximum in the displacements caused by xenon for a dose of $10^{16}$ Xe $cm^{-2}$ of about 25 displacements per atom (dpa). The dpa-level caused by the helium implantation is too small (<0.1 dpa) to be depicted in the figure. According to TRIM, helium is implanted in the centre of the damaged layer produced by the xenon implantation.

Yu et al. have compared TRIM calculations for 400 keV, 10° tilted xenon, with Rutherford backscattering measurements (RBS) and TEM measurements [10]. According to Yu's TRIM calculations, the projected range of 400 keV Xe-ions is 90 nm. However, it was measured by cross-sectional TEM that the thickness of the amorphous layer is 165 nm at a dose of $10^{16}$ Xe $cm^{-2}$. TEM observation gives a thickness of 155 nm for an amorphous spinel layer created by the implantation of 340 keV $Xe^{2+}$ ions [13]. This is according to their TRIM calculations at the end of both xenon ion and damage range. From the measurements presented in Refs. [10,13], we may conclude that the amorphous layer ends just after the maximum of the displacements as calculated by TRIM.

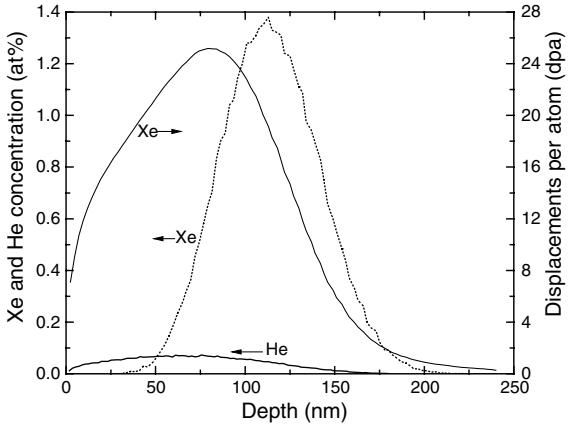


Fig. 1. Results of TRIM calculations for xenon ($10^{16}$ Xe $cm^{-2}$) and helium ($10^{15}$ He $cm^{-2}$) in spinel. The displacements caused by helium ions are negligible. Displacement energies of 30/30/60 eV for Mg/Al/O were used.

The sample used in our investigation, can be more or less compared with the sample described in Ref. [10], though our xenon implantation energy is higher (450 keV vs. 400 keV), thus we expect to find an amorphous layer with a thickness slightly larger than 165 nm. In the analysis, we should also take into account the possibility of channelling of xenon; part of it might be implanted deeper than predicted by TRIM.

The calculations for helium are performed for spinel without xenon, however, TRIM calculations for helium in spinel with an addition of 1.5% xenon show negligible differences compared to spinel without xenon. The presence of xenon and the amorphous structure will influence the helium path, the damage will block channelling, and xenon ions will scatter the helium.

A larger volume (31%) for amorphous spinel (i.e. a lower density), compared to crystalline spinel has been reported [14]. Finally, the results presented in Fig. 1 have not been corrected for sputtering. For a sputtering coefficient of 9 atoms/ion, the total surface sputtered off the sample due to the xenon implantation is about 8.5 nm. Due to sputtering the implantation profile will flatten slightly, and the maximum of this profile is shifted slightly towards the surface.

RBS-measurements for the present sample were performed at Los Alamos National Laboratories and are shown in Fig. 2. The RBS spectrum for spinel with only

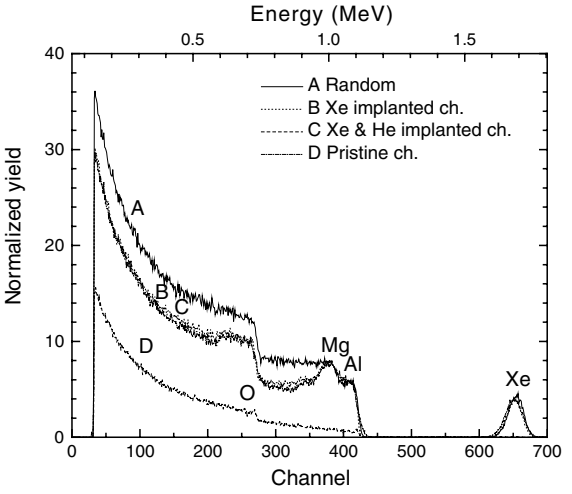


Fig. 2. RBS measurements for spinel: (a) random pristine spinel, (b) xenon implanted spinel; (1 1 1) channelling direction, (c) xenon and helium implanted spinel; (1 1 1) channelling direction, (d) pristine spinel; (1 1 1) channelling direction.

xenon and spinel with xenon and helium are almost identical, as the damage caused by helium is negligible compared to the damage caused by xenon (Fig. 1). The magnesium and aluminium signal for the amorphous spinel reach the random level. The oxygen shoulder will remain below the random level even if the oxygen sublattice becomes entirely disordered (amorphous). This is because the helium ion beam channels below the damage layer and this reduces the RBS yield for backscattered energies between the low end of the magnesium peak and the surface position of the oxygen peak. The oxygen damage peak is then superimposed on this low channelling background. In the case of the random spectrum, the yield is high at all backscattered energies.

### 2.3. Desorption experiments

Two desorption apparatus were used to perform desorption experiments, one apparatus is based on the principle of the detection of gases in a flow effusing from a crucible (the Knudsen cell (KCM, Knudsen Cell Measurements) [15,16] of the Institute for Transuranium Elements), the second apparatus is based on the partial pressure increase in a small oven (the thermal helium desorption facility (THDS) of the Interfaculty Reactor Institute). Several samples have been investigated in one of the two systems, as described in Table 1. The sample sizes and the corresponding helium contents are also given in the table. In the THDS, samples were annealed in vacuum with a ramp rate of either 60 K min$^{-1}$ (sample VII) or 180 K min$^{-1}$ (sample VIII) up to 1300 K, or in several annealing steps, where the maximum temperature was increased by 50 K for each measurement (i.e. 300–500, 300–550 K etc.). Immediately after reaching the maximum temperature, the sample was cooled down (sample IX). A similar approach for helium in silicon is described in Ref. [17].

In the KCM experiments, the release of both helium and xenon (samples IV–VI) and only xenon (sample III) were monitored. The samples were annealed under vacuum with a heating rate of 30 K min$^{-1}$. In both systems, the mass signal was monitored with a quadrupole mass spectrometer, and the measured temperatures have been corrected for a delay in the temperature between the crucible and the sample, as spinel is almost transparent for infrared radiation. The helium release curves obtained with both systems will be compared.

### 2.4. Positron beam analysis

The positron beam analysis (PBA) technique was applied on:

Table 1
Overview of investigated samples and the applied analyses

| Sample | Type[a] | Experiment | Annealing | Number of implanted He-ions | Surface (mm$^2$) | $T_{max}$ (K) of peak $He_A/Xe_A$ | $T_{max}$ (K) of peak $He_B/Xe_B$ | Peak content (%) $He_A/He_B/He_C$ |
|---|---|---|---|---|---|---|---|---|
| I | 1 | PBA | RT | | | | | |
| II | 2 | PBA | RT | | | | | |
| III | 2 | KCM | 0.5 K s$^{-1}$ | | 3.16 | –/1066 | –/1249 | |
| IV | 3 | KCM | 0.5 K s$^{-1}$ | $2.6 \times 10^{13}$ | 2.64 | 690/1066 | 758/1249 | |
| V | 3 | KCM | 0.5 K s$^{-1}$ | $2.1 \times 10^{13}$ | 2.08 | 690/1066 | 758/1249 | |
| VI | 3 | KCM | 0.5 K s$^{-1}$ | $3.4 \times 10^{13}$ | 3.42 | 690/1066 | 758/1249 | |
| VII | 3 | THDS | 1 K s$^{-1}$ | $3.1 \times 10^{13}$ | 3.05 | 627/– | 741/– | 44/56/0 |
| VIII | 3 | THDS | 3 K s$^{-1}$ | $3.9 \times 10^{13}$ | 3.87 | 615/– | 745/– | 32/54/14 |
| IX | 3 | THDS | Stepwise | $4.6 \times 10^{13}$ | 4.64 | | | 42/50/8 |
| X | 3 | PBA | See Fig. 7 | | | | | |

[a] Sample type 1: virgin spinel; sample type 2: spinel amorphized with xenon; sample type 3: amorphous spinel implanted with helium.

- a virgin single-crystal sample (sample I);
- spinel with an amorphous layer (spinel with xenon, sample II);
- amorphous spinel implanted with helium (sample X).

For all these samples, investigations have been performed at room temperature (RT). For the last sample (X), the defect evolution during thermal annealing has also been studied. The sample was annealed in vacuum for 10 min at a constant temperature and then cooled to RT before starting the measurement. The equipment for heating the sample is described in Ref. [18], and the annealing of the samples has been performed in vacuum by making use of electron bombardment.

The generation and evolution of defects can be monitored with the PBA technique. A mono-energetic positron beam was used, and the energy of the positrons was varied between 0.1 and 25 keV. With increasing positron implantation energy, the depth increases at which a positron is thermalized and ultimately annihilates. In this way, depth-dependent defect information can be obtained [19]. The thermalized positron will annihilate with an electron present in the material and mostly two photons will be emitted with an energy of 511 keV, when the electron has zero momentum. If the electron carries momentum, the energy will deviate from 511 keV because of Doppler broadening. One of the two photons is detected with a high-resolution germanium detector and this event is stored in a pulse height analysed spectrum. After accumulation of about $10^6$ events in the 511 keV photo-peak, the broadening of this peak, due to the Doppler effect caused by the momentum of the annihilating electron, is determined and quantified by the so-called *S*- and *W*-parameters. By defining the appropriate windows in the photo peak, the *S*-parameter is sensitive to the fraction of annihilations with low momentum electrons and the *W*-parameter to the fraction of high momentum electrons.

In general, the annihilation of a positron with a valence electron (low momentum) causes less broadening than the annihilation with core electrons. Taking into account that a positron annihilating in a local open volume (such as a defect or defect agglomerate) has a lower probability to annihilate with core electrons, we therefore expect the *S*-parameter to be larger as compared to the *S* of a defect-free sample. For the value of the *W*-parameter the opposite is observed [19]. In the analysis described in this article we will only use the *S*-parameter.

## 3. Results and discussion

### 3.1. Helium and xenon desorption

The results of the helium and xenon desorption experiments are shown in Fig. 3, where the THDS results

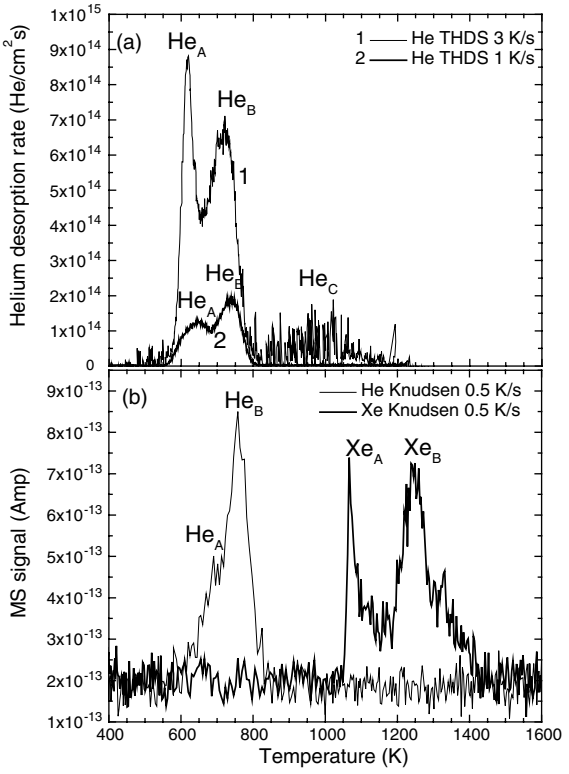


Fig. 3. Results of helium and xenon release experiments. In the upper figure (a), the helium release as-measured with THDS is shown (samples VII and VIII) while in the lower figure (b) the results helium and xenon release of the Knudsen cell experiments are shown (sample IV). $He_A$, $He_B$, $He_C$, $Xe_A$ and $Xe_B$ indicate the different release stages for helium and xenon.

(only helium release) are displayed in the upper figure (samples VII and VIII) and the Knudsen cell results (both helium and xenon release) in the lower figure (sample IV). The data are plotted vs. temperature to facilitate an easy comparison between the different heating rates applied. For both investigation methods most of the helium is released between 600 and 800 K and xenon is released between 1050 and 1500 K.

In the figures, it can clearly be seen that helium is released in two stages ($He_A$ and $He_B$), which is also observed for the xenon release (Fig. 3(b)). For sample VIII, also a third stage releasing a minor amount of helium is observed ($He_C$), although this is not observed for sample VII and also not with KCM. However, the third stage is also observed for sample IX, which will be discussed later. The xenon release starts very suddenly at 1050 K; this might be an effect of sweeping out during recrystallization. The release of $He_C$ occurs in the same temperature range as the first part of the xenon release, which makes the hypothesis of sweeping the gas during recrystallization stronger. It could also be possible that

the release of the helium in $He_C$ is caused by burst release due to thermally induced flaking [6], however, this has not been confirmed by SEM investigations of the as-annealed samples. The release stages $He_A$ and $He_B$ might be explained by helium release from the zone where no xenon is implanted (close to the surface, $He_A$) and helium release from the zone where also xenon is present ($He_B$). This fits approximately to the amounts of helium trapped in both zones. The fractions of helium released in each peak ($He_A$, $He_B$ and $He_C$) are given in Table 1 as well. It should be noted that the KCM results are given in Ampere. As there is no calibration of helium and xenon at the moment, this is the direct output signal of the mass spectrometer, which is linear with the amount of ions. An overview of relevant temperatures is also given in Table 1.

The results of the partial annealing experiment, as performed with THDS with a heating rate of 3 K $s^{-1}$ (sample IX) are shown in Fig. 4. In this figure, the spectra are labelled with characters A–L, which correspond to the data given in Table 2. In addition, the release rates during both heating and cooling are shown. Again, we can distinguish three release stages, indicated by $He_A$, $He_B$ and $He_C$. The maximum release is observed at a temperature of about 850 K. For the ramp annealing experiments, most of the helium is released at this temperature. The helium release in the partial annealing starts at about 600 K, which corresponds to the first release peak observed in the ramp annealing experiments. For successive temperature steps, the temperature at which the helium release starts, is somewhat lower than the maximum temperature of the previous annealing step. In case of partial annealing, helium is retained up to the same temperatures as observed for sample VIII, annealed at 3 K $s^{-1}$. The fact that at lower ramping rate no release at this temperature is seen is due to the signal/background ratio, which becomes too low as the helium release per unit of time is reduced. From the experiments where the sample has been annealed stepwise, information on the release mechanisms can be obtained by looking at the first part of the release curves [17].

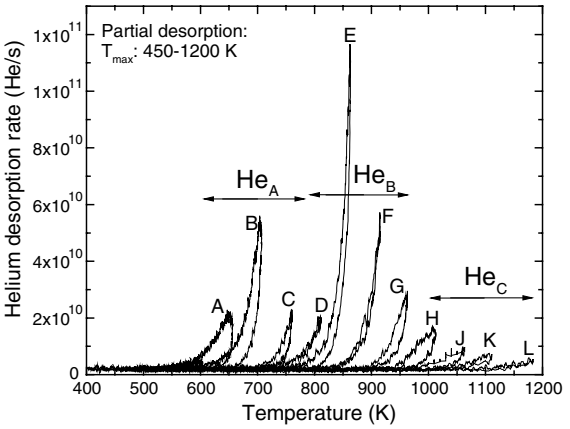


Fig. 4. Partial helium desorption for sample IX. The applied heating rate was 3 K $s^{-1}$. The letters A–L indicate the annealing step as shown in Table 2. $He_A$, $He_B$ and $He_C$ are indicators for the three different release stages observed.

When the release is a first-order desorption process, the time ($t$) dependent release can be described as:

$$\frac{dN}{dt} = -Nf \tag{1}$$

with $N(t)$ the number of helium retained in the sample, $f = f_0 \exp(-Q/kT)$ the temperature dependent release frequency, $k$ is the Boltzmann constant, $T$ the temperature and $Q$ is the activation enthalpy of diffusion. If we consider only the first part of the release curve, the change in $N$ is very small, so we can assume $N$ to be constant and equal to $N_{0,i}$, which is the amount of helium at the begin of the annealing step $i$. Then, plotting the logarithm of the release rate vs. $1/T$ will show Arrhenius behaviour. From the slopes of the curves the activation enthalpy $Q$ can be derived. The pre-exponential factors

Table 2
Results of the partial annealing THDS experiments of sample IX as shown in Figs. 4 and 5

| Annealing step | $T_{max}$ (K) | Helium content (%) | $Q$ (eV) | $\delta Q$ (eV) (fitting error) | Attempt frequency ($s^{-1}$) |
|---|---|---|---|---|---|
| A | 656 | 100.0 | 2.04 | 0.19 | $1.66 \times 10^{14}$ |
| B | 707 | 97.4 | 2.05 | 0.08 | $2.24 \times 10^{13}$ |
| C | 760 | 84.1 | 1.71 | 0.07 | $1.70 \times 10^{9}$ |
| D | 811 | 58.4 | 2.94 | 0.18 | $2.88 \times 10^{15}$ |
| E | 863 | 51.9 | 2.65 | 0.14 | $5.62 \times 10^{13}$ |
| F | 915 | 44.8 | 2.73 | 0.10 | $1.74 \times 10^{13}$ |
| G | 963 | 19.7 | 2.52 | 0.09 | $1.05 \times 10^{11}$ |
| H | 1012 | 8.3 | 2.82 | 0.16 | $1.15 \times 10^{12}$ |
| J | 1063 | 3.6 | 1.80 | 0.14 | $1.35 \times 10^{6}$ |
| K | 1111 | 1.2 | 2.02 | 0.17 | $6.76 \times 10^{6}$ |
| L | 1183 | 0.2 | 1.58 | 0.14 | $5.75 \times 10^{4}$ |

$f_{0,i}$ of the different partial annealing steps ($i$) can be derived by calculating:

$$f_{0,i} = \left(\frac{dN}{dt}\right)\left(\frac{1}{N_{0,i}}\right)\exp\left(\frac{Q}{kT}\right). \quad (2)$$

In this assumption $N_{0,i}$ is the initial fraction of helium present in the sample at the beginning of the $i$th annealing step.

The Arrhenius behaviour (release rate vs. $1/T$) has been plotted in Fig. 5. In each curve, the part, which has been used for determining the activation enthalpy, has been indicated. From the plot, the activation enthalpy for diffusion can be obtained from the slopes of the curves if only the initial part of each desorption curve is used. In Table 2, for each of the annealing steps, the following data are given: The maximum annealing temperature ($T_{max}$) for the annealing step (these data are already corrected for the delay in temperature between sample and crucible), the fraction of initially implanted helium ($4.64 \times 10^{13}$ ions) which is still present at the beginning of the annealing step, the activation enthalpy ($Q$) as determined from the part of the slope as indicated in Fig. 5, the error in the activation enthalpy ($\delta Q$) only due to the fitting, and the value of the calculated attempt frequencies $f_{0,i}$ (Eq. (2)). The calculated values for the activation enthalpy $Q$ and the frequency pre-factor $f_{0,i}$ are shown in Fig. 6. One can clearly distinguish the three different regions in the figure as indicated with $He_A$, $He_B$ and $He_C$. The frequencies found for the two stages of desorption $He_A$ and $He_B$ are close to what is expected for first-order desorption, namely of the order of the jump frequencies for solids [20]. The $He_C$ desorption has a very low pre-exponential factor which might indicate a multi-step activated process like diffusion or desorption from helium bubbles.

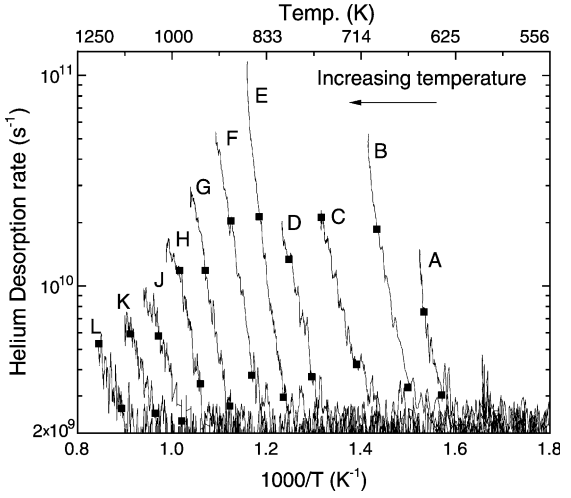


Fig. 5. Arrhenius plot for THDS results as shown in Fig. 4. The squares in the figure indicate the parts of the curves, which have been used for the calculation of the activation enthalpies. The letters A–L indicate the annealing step as given in Table 2 and are also shown in Fig. 4.

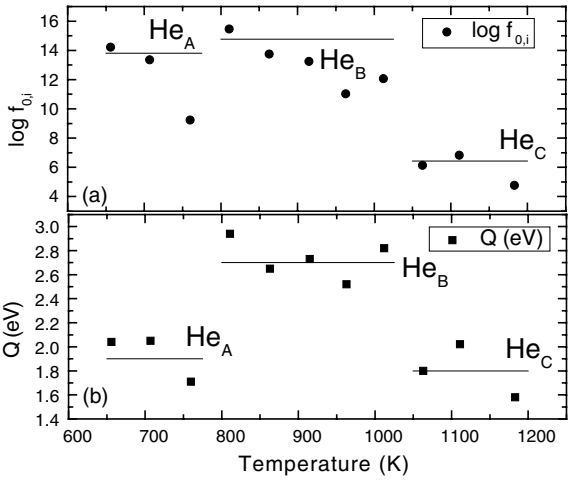


Fig. 6. The values for frequency pre-factor $f_{0,i}$ (a), and activation enthalpy $Q$ (b) as calculated from the data presented in Figs. 4 and 5. The horizontal lines indicate the average value per helium release peak.

Three different activation enthalpies are derived for the curves in the slope: $(1.9 \pm 0.2)$ eV for $He_A$, $(2.7 \pm 0.3)$ eV for $He_B$ and $(1.8 \pm 0.3)$ eV for $He_C$. The errors in the activation enthalpy presented above only apply to the error in the fitting, where the error in background subtraction is included; however, the real error in activation enthalpy is caused by more parameters. Although we corrected our measured temperature data for the temperature delay between crucible and sample, we will still have some error in temperature ($\pm 10$ K). The real error in activation enthalpy will thus be larger than the errors given above.

### 3.2. Positron beam analysis

PBA-experiments were performed at RT on a virgin spinel single-crystal (sample I) and a spinel crystal with an amorphous layer (sample II). The helium implanted amorphous layer (sample X) was investigated by PBA at RT and after annealing up to certain temperatures. The applied heating schedule is presented in Fig. 7. For each annealing step, the sample is heated up to the desired temperature within several minutes. After the temperature is kept constant for about 10 min, the sample is cooled down to RT before the positron measurement is started. The PBA measurements on the as-helium irradiated amorphous spinel (sample X) reveals a somewhat lower $S$-value as compared to the amorphous sample without helium (sample II). The assumption is that

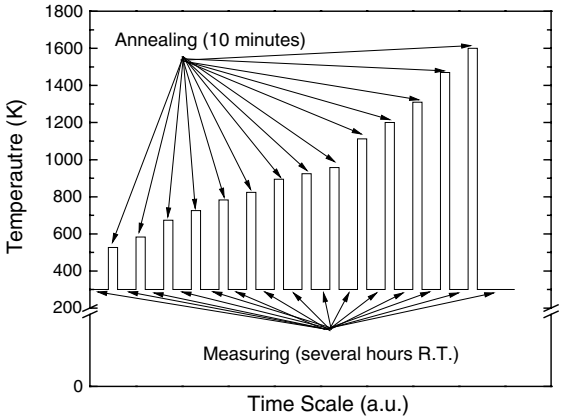


Fig. 7. The applied heating schedule for the PBA measurements. For each annealing step, the sample is heated up to the desired temperature within several minutes. After the temperature is kept constant for about 10 min, the sample is cooled down to RT (no forced cooling), before the positron measurement is started.

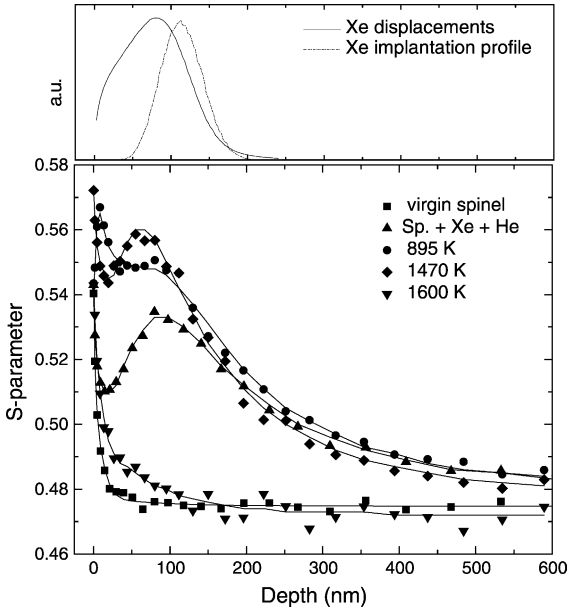


Fig. 8. The as-measured (symbols) *S*-parameter and the results obtained with VEPFIT (drawn lines) vs. the depth for several annealing temperatures. The upper part of the figure shows the results as calculated with TRIM for comparison.

helium fills up part of the open volumes in the amorphous structure.

In Fig. 8, the as-measured *S*-parameter vs. the depth in the material is shown for virgin (unimplanted) spinel (sample I) and the amorphous spinel with helium after various annealing stages. In the top part of the figure, also the xenon displacements and the xenon ion distribution are shown in arbitrary units, as calculated with TRIM. The depth at which a local maximum in the *S*-parameter is seen for the as-irradiated sample agrees quite well with the position of the maximum in the xenon displacement profile. From this can be concluded that the TRIM calculations agree well with the real implantation data and channelling effects can be neglected in our case. It can be seen that in the xenon and helium implanted area, the *S*-parameter increases after annealing up to temperatures of 1470 K. Above 1600 K, the *S*-parameter profile reaches the curve for pristine spinel.

Fig. 9 shows the fitting results as obtained with the program VEPFIT [21,22] where a three-layer model has been used to describe the amorphous region (layers 1 and 2) on top of the bulk material (layer 3). The reason to split the xenon and helium implanted region into two layers is based on the observation that, with increasing positron depth, the *S*-parameter first drops, then increases to a maximum whereafter it gradually decreases to the *S*-value of the bulk. The *S*-parameters and the upper boundary of the layers 1 and 2 and the *S*-parameter of the bulk are the fitting parameters in the model. Fitting has been performed on the data obtained after xenon and helium implantation and after annealing at 895 and 1470 K. The results in this graph are presented numerically in Table 3 where the border of each zone is given, not its thickness. From the fittings with the VEPFIT-program, the following observations can be made (see Fig. 9 and Table 3):

- At RT, the first layer has a width of about 50 nm, which is according to TRIM the part where only

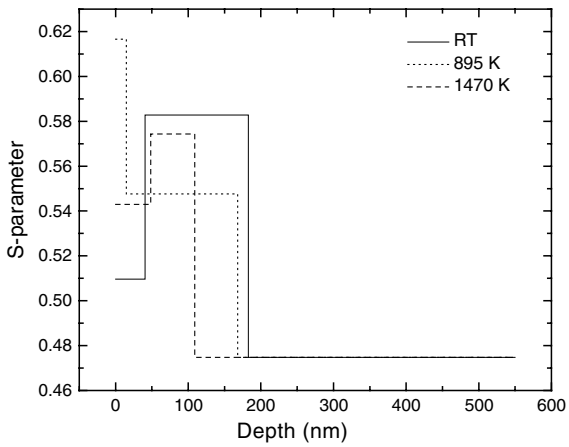


Fig. 9. The *S*-parameter as fitted with VEPFIT with a three-layer model for three different annealing stages (RT, 895 and 1470 K). The third layer is the bulk, which is the same for the three different temperatures.

Table 3
Fitted layer boundary and *S*-parameters per layer with a three-layer model using VEPFIT for sample X annealed at the indicated temperatures

| Annealing temperature (K) | Upper boundary layer 1 (nm) | Upper boundary layer 2 (nm) | *S* layer 1 | *S* layer 2 | *S* bulk (layer 3) |
|---|---|---|---|---|---|
| 300 | 40.5 | 182.9 | 0.5097 | 0.5828 | 0.4748 |
| 895 | 14.8 | 168.0 | 0.6166 | 0.5476 | 0.4748 |
| 1470 | 48.3 | 109.0 | 0.5430 | 0.5743 | 0.4748 |

helium and no xenon are implanted. This zone has a low *S*-parameter, the second zone has a high *S*-parameter, and its depth location agrees very well with the xenon displacement profile, and thus with the thickness of the amorphous layer reported in Ref. [10].

- For the annealing at 895 K, we can see that the first layer has become much smaller and its *S*-parameter has increased significantly; this corresponds to a small layer under the surface with large open volumes. The end position of the second layer has not changed much compared to the RT sample; for this layer, there has been a drop in the *S*-parameter compared to the second zone at RT. Helium release has occurred, but xenon is still immobile.
- After annealing at 1470 K, we see that the first zone has approximately the same width as the first zone at RT. The *S*-parameter of this zone is about the same as the *S*-parameter of the second zone after annealing at 895 K, the second zone at this temperature has a high *S*-parameter comparable to layer 2 at RT, xenon release has occurred leaving open volumes behind.

In Fig. 10, for three indicated depths in the material, the as-measured *S*-parameter is plotted vs. the annealing temperature. From Fig. 8, we can see that at a depth of 8.5 nm we are looking very close under the surface and in this region we observe a large increase in the *S*-value at 895 K. At a depth of 24 nm we are looking in the regime where only helium and no xenon is present. A depth of 95 nm is the region with the maximum of the displacements caused by the xenon. Up to 600 K, we do not observe a large change in the *S*-parameter at any of the selected depths. From the helium desorption experiments we know that there has been no helium release at these temperatures.

We can distinguish five different stages in the change of the *S*-parameter vs. temperature beyond 600 K; these changes are numbered in Fig. 10.

1. In stage 1, between 700 and 950 K, the *S*-parameter at 9 and 24 nm increases while the *S*-parameter at 95 nm stays more or less constant. The increase in *S*-parameter for the two lower depths can be explained by the release of helium and the clustering of defects.

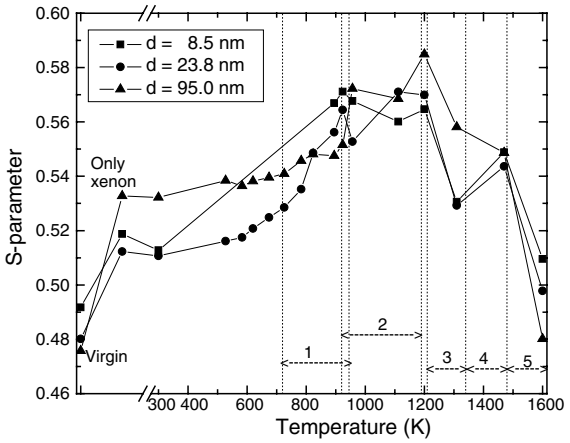


Fig. 10. As-measured *S*-parameter vs. the annealing temperature for three different depths. The 'virgin' point is for an unimplanted, unannealed spinel single crystal. The numbers 1–5 refer to the different stages observed in the *S*-profile as explained in the text.

2. In stage 2, between 920 K and 1200 K, the near-surface *S*-parameter stays more or less constant while the *S*-parameter in the deeper regions increases. In this temperature interval, helium has been released; this is the temperature interval where we observe the first release peak of xenon. Recrystallization has occurred leaving large defect clusters behind. TEM observations have shown [13] that recrystallization of the amorphous surface layer takes place in the temperature interval between 883 and 1128 K.
3. In stage 3, between 1200 and 1350 K, we observe a large drop in the *S*-value for both the near surface region (8.5 nm) and the deeper regions. We expect that this is due to defect recovery after recrystallization.
4. In stage 4, between 1350 and 1480 K, we observe an increase in the *S*-value in the region where xenon has been implanted. According to literature [13], the xenon stays immobile up to 1370 K. In this stage, according to the Knudsen cell measurements (KCM) we expect that xenon is released, leaving open volumes behind, by which the increase in the *S*-parameter in the xenon implanted zones can be explained.
5. Finally, in stage 5, we see after annealing up to more then 1600 K that the *S*-values reach the level

of pristine spinel, and all defects have been removed from the sample.

## 4. Comparisons with the helium and xenon behaviour in crystalline spinel

### 4.1. Helium release

We have observed three stages for helium release from amorphous spinel:

- $He_A$ at about 620 K with an activation enthalpy of 1.9 eV;
- $He_B$ at about 740 K with an activation enthalpy of 2.7 eV;
- $He_C$ at about 1000 K with an activation enthalpy of 1.8 eV, probably caused by sweeping out during recrystallization.

In the literature, no helium implantation experiments could be found where helium was implanted in spinel at the same depth and dose as was the case in our samples. Thus we will try to compare our release curves with data from the literature where about the same implanted dose has been used.

Neeft et al. [8] have implanted 900 keV $^3$He-ions in both single-crystal and polycrystalline spinel with different doses. It was observed that the helium release took place in at least two stages in a wide temperature interval ranging from 600 to 1600 K, where the release temperature range depends both on the implanted dose and whether the spinel is single-crystal or polycrystalline. It was concluded that the helium at higher doses is released at lower temperatures. If the release temperature gets lower for a higher implanted dose (more damage), then it would fit in our experiments where we have introduced much more damage than in the cases presented in Ref. [8].

Single crystals of spinel were implanted with 30 keV $^3$He-ions, with four different doses, varying between $6.2 \times 10^{15}$ and $53 \times 10^{15}$ He cm$^{-2}$ [9]. Helium release was observed in three stages; between 550 and 700 K, between 750 and 1100 K and between 1100 and 1400 K. Secondly, spinel single-crystals were irradiated with $\alpha$-particles of 4.5 MeV originating from an $^{241}$Am-source. Two activation enthalpies are quoted: 1.8 eV attributed to helium interstitial diffusion and 2.4 eV attributed to helium release from vacancy clusters.

The temperatures for the THDS experiments described in the present article, have been calibrated with a thermocouple mounted to the sample, however, the temperature data for the experiments described in Refs. [8,9] are not corrected for the delay in temperature between sample and crucible (normally the crucible temperature is monitored). Therefore it might be that the measured activation enthalpies are somewhat overestimated.

If we compare the helium release data for amorphous spinel to data for crystalline spinel we see that in general helium is released with a somewhat higher activation enthalpy than in the amorphous case. Most of the helium is released below the recrystallization temperature. It is likely that amorphized spinel contains deeper traps for helium than crystalline spinel. Also it might be expected that xenon atoms embedded in amorphous spinel generate sufficient open space to trap helium stronger than in amorphous spinel without xenon.

### 4.2. Xenon release

We could not find information in the literature, on annealing experiments for xenon implanted spinel. However, Matzke [23] has measured the xenon release from spinel in air to start at 1800 K, thus at much higher temperatures as was the case in our experiments. Turos et al. [24] have investigated the damage caused by xenon and krypton implantations. After annealing at 775 K, a reduction of the number of defects resulting in a decrease of almost 50% of the Al- and O-damage peaks was observed with RBS for an implanted dose of $1 \times 10^{15}$ Kr cm$^{-2}$. For crystalline spinel, an important recovery of defects is observed at this temperature for this implanted dose, however, this effect was not observed for an implanted dose of $7 \times 10^{15}$ Kr cm$^{-2}$. Our RBS measurements have only been performed on unannealed specimens. From PBA we did not observe a defect recovery at these temperatures. The xenon release from amorphized spinel starts most likely at the recrystallization temperature. Then part of the xenon is swept out, which can be seen as a very sharp rise in the xenon release signal. The rest of the xenon is released via diffusion processes, as would be the case in crystalline spinel.

## 5. Conclusions and final remarks

Spinel was amorphized by the implantation of $1 \times 10^{16}$ Xe cm$^{-2}$ of 450 keV at cryogenic temperatures (100 K). Then, 14 keV $He^+$-ions were implanted in the sample up to a total implanted dose of $1 \times 10^{15}$ He cm$^{-2}$. The helium was implanted in the centre of the amorphous zone. The maximum helium concentration amounted to 0.07 at.% is found at a depth of 77 nm.

The release profile of helium under thermal annealing has been monitored by KCM and THDS. Helium is released in at least two stages, with peak maxima at about 615 and 720 K. The activation enthalpies of the different release stages could be determined from the measured partial desorption spectra. These are 1.9, 2.7 and 1.8 eV for stages 1 ($He_A$), 2 ($He_B$) and 3 ($He_C$), re-

spectively, with frequency factors of $6 \times 10^{13}$, $6 \times 10^{14}$ and $3 \times 10^{6}$ $s^{-1}$. The two largest frequency factors given are typical for first-order desorption, the smaller value could be explained by a multi-step activated process like diffusion or desorption from helium bubbles. Xenon release starts very suddenly at 1050 K. This could be an effect of sweeping out during recrystallization. Then, the second xenon release peak is observed with a maximum at about 1280 K, all helium has been released at this temperature.

PBA experiments have been performed at RT and after various annealing steps. The PBA data have been analysed using the VEPFIT code, where a three-layer model was used. At RT, these three-layers, corresponding to amorphized spinel without xenon, amorphized with xenon and the substrate agree very well with data calculated with TRIM.

## Acknowledgements

The authors like to thank Dr A.V. Fedorov from IRI Delft for his assistance in the helium desorption experiments, and J.Y. Colle, F. Capone and J.-P. Hiernaut for their assistence in the Knudsen cell measurements.

## References

[1] Hj. Matzke, J.L. Whitton, Can. J. Phys. 44 (1966) 995.
[2] K.E. Sickafus, A.C. Larson, N. Yu, M. Nastasi, G.W. Hollenberg, F.A. Garner, R.C. Bradt, J. Nucl. Mater. 219 (1995) 128.
[3] T. Wiss, Hj. Matzke, Radiat. Eff. 31 (1999) 507.
[4] R.J.M. Konings, R. Conrad, G. Dassel, B.J. Pijlgroms, J. Somers, E. Toscano, J. Nucl. Mater. 282 (2000) 159.
[5] E.A.C. Neeft, R.J.M. Konings, H. Schut, A.V. Federov, in: Proceedings of the 9th CIMTEC Advances in Science and Technology, vol. 24, Italy, 14–19 June, 1998, p. 531.
[6] R. Fromknecht, J.P. Hiernaut, Hj. Matzke, T. Wiss, Nucl. Instrum. and Meth. B 166&167 (2000) 263.
[7] T. Wiss, Hj. Matzke, V.V. Rondinella, T. Sonoda, W. Assmann, M. Toulemonde, C. Trautmann, Prog. Nucl. Energy 38 (2001) 281.
[8] E.A.C. Neeft, A. van Veen, R.P.C. Schram, F. Labohm, Prog. Nucl. Energy 38 (2001) 287.
[9] E.A.C. Neeft, R.P.C. Schram, A. van Veen, F. Labohm, A.V. Federov, Nucl. Instrum. and Meth. B 166 (2000) 238.
[10] N. Yu, K.E. Sickafus, M. Nastasi, Philos. Mag. Lett. 70 (1994) 235.
[11] S. Zinkle, Hj. Matzke, V.A. Skuratov, in: MRS Symposium Proceedings, vol. 540, 1999, p. 299.
[12] J.F. Ziegler, J.P. Biersack, U.L. Littmark, The Stopping Power and Range of Ions in Solids, Pergamon, New York, 1985, The calculations presented in this paper used the SRIM-2000 version.
[13] I.V. Afanasyev-Charkin, R.M. Dickerson, D.W. Cooke, B.L. Bennett, V.T. Gritsyna, K.E. Sickafus, J. Nucl. Mater. 289 (2001) 110.
[14] S. Chen, M. Yan, Philos. Mag. Lett. 73 (1995) 51.
[15] F. Capone, Y. Colle, J.P. Hiernaut, C. Ronchi, J. Phys. Chem. A 103 (1999) 10899.
[16] V.V. Rondinella, T. Wiss, Hj. Matzke, J.-P. Hiernaut, R. Fromknecht, Advances in Science and Technology: Mass and Charge Transport in Inorganic Materials, Fundamentals to Devices, in: P. Vincenzini, V. Buscaglia (Eds.), Techna Srl., vol. 20, part A, 2000, p. 499.
[17] S. Godey, E. Ntsoenzok, T. Sauvage, A. van Veen, F. Labohm, M.F. Beaufort, J.F. Barbot, Mat. Sci. Eng. B 73 (2000) 54.
[18] H. Schut, A. van Veen, A. Rivera, M.A. van Huis, A. Alba García, R. Escobar Galindo, Appl. Surf. Sci. 194 (2002) 239.
[19] A. van Veen, H. Schut, P.E. Mijnarends, Depth-profiling of subsurface regions, interfaces and thin films, in: P. Coleman (Ed.), Positron Beams and their Applications, World Scientific, Singapore, 2000, Chapter 6, p. 191.
[20] P.G. Shewmon, Diffusion in Solids, McGraw-Hill Book Company, 1963.
[21] A. van Veen, H. Schut, M. Clement, J.M.M. de Nijs, A. Kruseman, M.R. IJpma, Appl. Surf. Sci. 85 (1995) 216.
[22] H. Schut, A. van Veen, Appl. Surf. Sci. 85 (1995) 225.
[23] Hj. Matzke, unpublished results.
[24] A. Turos, Hj. Matzke, A. Drigo, A. Sambo, R. Falcone, Nucl. Instrum. and Meth. B 113 (1996) 261.